High-Precision Multidimensional Photosensor Based on Hybrid Optofluidic Microbubble Resonator

Bing DUAN[1], Xuan ZHANG[1], Xiaochong YU[2*], Yixuan ZHAO[1], Jinhui CHEN[3], Yongpan GAO[1], Cheng WANG[4], and Daquan YANG[1*]

[1]*State Key Laboratory of Information Photonics and Optical Communications, Beijing University of Posts and Telecommunications, Beijing 100876, China*

[2]*School of Physics and Astronomy; Applied Optics Beijing Area Major Laboratory; Key Laboratory of Multiscale Spin Physics, Ministry of Education, Beijing Normal University, Beijing 100875, China*

[3]*Institute of Electromagnetics and Acoustics, Xiamen University, Xiamen 361005, China*

[4]*Department of Electrical Engineering; State Key Laboratory of Terahertz and Millimeter Waves, City University of Hong Kong, Hong Kong 999077, China*

[*]Corresponding authors: Xiaochong YU and Daquan YANG E-mails: yuxc@bnu.edu.cn and ydq@bupt.edu.cn

Abstract: Optical microcavities combined with different materials have inspired many kinds of functional photonic devices, such as lasers, memories, and sensors. Among them, optofluidic microbubble resonators with intrinsic micro-channels and high-quality factors (high-Q) have been considered intriguing platforms for the combination with liquid materials, such as the hydrogel and liquid crystal. Here, we demonstrate a water-infiltrated hybrid optofluidic microcavity for the precise multidimensional measurement of the external laser field. The laser power can be precisely measured based on the photo-thermal conversion, while the wavelength-resolved measurement is realized with the intrinsic absorption spectrum of water. Empowered by machine learning, the laser power and wavelength are precisely decoupled with almost all predictions falling within the 99% prediction bands. The correlation coefficient R^2 of the laser power and wavelength are as high as 0.999 85 and 0.999 54, respectively. This work provides a new platform for high-precision multidimensional measurement of the laser field, which can be further expanded to arbitrary band laser measurement by combining different materials.

Keywords: Hybrid microcavity; multidimensional laser measurement; machine learning

Citation: Bing DUAN, Xuan ZHANG, Xiaochong YU, Yixuan ZHAO, Jinhui CHEN, Yongpan GAO, *et al*., "High-Precision Multidimensional Photosensor Based on Hybrid Optofluidic Microbubble Resonator," *Photonic Sensors*, 15(3), 250310.

1. Introduction

Optical microcavities can significantly enhance the light-matter interaction due to the high-quality factors (high-Q) and small mode volume, spurring applications in nonlinear optics [1–4], optomechanics [5–8], quantum electrodynamics (QED) [9–11], optical communications [12], optical frequency combs [13–14], lasing [15–17], and sensing [18–21]. In particular, the interplay between optical microcavities and functional materials has drawn considerable attention in new photonic devices, such

Received: 24 May 2024 / Revised: 10 January 2025

DOI: 10.1007/s13320-025-0768-y
Article type: Regular

as electro-optic modulators [22], optical memories [23], and optical switches [24]. Among them, the optofluidic microbubble resonators (OMBRs) are an ideal platform for the combination with liquid materials due to the natural micro-channels and high-Q factor [25]. By filling with different materials, OMBRs have facilitated various applications [26, 27]. For example, the integration of OMBRs with high-gain media has inspired low-threshold microcavity lasers [28–30]. The detection limits of OMBR-based sensors have reached the level of a single biomolecule in an aqueous environment by integrating surface plasma [31, 32]. Furthermore, this system has also been used for the detection of the ultralow concentration biochemical solution and gas, as well as for the operando monitoring of transition dynamics of phase change materials [33]. Remarkably, the OMBR not only is available for biochemical materials sensing [34–37], but also exhibits the great potential for the high precision measurement of external physical quantities, e.g., temperature, aerostatic pressure, ultrasound, and magnetic field [38–40]. Recently, precise laser measurement has attracted great attention from commercial applications to scientific research [41–44]. So far, there have been few demonstrations that these optical-cavity systems can be used for the multidimensional measurement of external laser fields. This is mainly due to the weak response of external lasers by conventional microcavity materials such as silicon dioxide and silicon nitride. In contrast, the hybrid microcavity combined with photosensitive materials or light-absorbing materials opens a new road for measuring the properties of the external light field. In addition, the water has an extremely broad absorption spectral range, covering the ultraviolet, infrared, and even terahertz wavelengths [45], which creates new opportunities for broadband laser measurement based on the optofluidic microcavity.

In this work, we demonstrate a novel technique for multidimensional laser measurement by using a water-infiltrated hybrid microcavity. The laser power can be precisely measured using photo-thermal conversion in a high-Q hybrid microcavity, while the wavelength-resolved measurement can be further achieved by leveraging the intrinsic absorption spectrum of water. As a proof of concept, we implement the laser measurement in the near-infrared band with a high-Q factor hybrid OMBR. Empowered by a three-layer perceptron neural network model, the power and wavelength of the external laser field are precisely decoupled. The average prediction errors of the power and wavelength are 2.16 μW and 1.43 nm, respectively, with almost all the predictions falling in the 99% prediction band. The values of the correlation coefficient R^2 of 0.999 85 and 0.999 54 are achieved for the laser power and wavelength, respectively. Although this work is just a proof of concept, the proposed water-infiltrated hybrid microcavity can be further expanded to mid-infrared and terahertz bands.

2. Fabrication and characterization

Figure 1(a) shows the schematic diagram of multidimensional laser measurement based on the hybrid microcavity. Here, the probe laser at the visible band is used to couple the light into the hybrid microcavity to excite resonant modes. The irradiation laser is the external laser to be measured, which is absorbed by the hybrid microcavity via an extra single-mode fiber. It is mentioned that the probe light power is about 20 μW, which is coupled into the microcavity via near-field and does not interfere with the irradiation free-space light. The OMBR with a diameter of ~80 μm and wall thickness of ~2 μm is fabricated with a silica hollow capillary through the “heat-and-expand” method [46]. When the irradiation laser illuminates the hybrid microcavity (near the coupling region) through the irradiation fiber [inset of Fig. 1(a)], the light is absorbed, leading to temperature changes

due to photo-thermal conversion. Consequently, the laser power and wavelength can be measured from the resonant mode shift of the hybrid microcavity. The conversion efficiency is mainly determined by the spot area of the irradiation laser. For a far-field Gaussian beam, an effective irradiation laser spot area is defined as [47]

$$A_{\text{eff}} = \frac{\pi\omega_0^2}{2} \tag{1}$$

where ω_0 is the radius of the far-field laser beam and can be obtained through $\omega_0 = d\theta/2$. Here, d is the distance between the hybrid microcavity and irradiation fiber, and θ is the far-field divergence angle and can be calculated from $\theta = 4\lambda/(\pi\text{MFD})$, where MFD is the mode field diameter and λ is the irradiation wavelength. Therefore, the laser spot area can be calculated by

$$A_{\text{eff}} = \frac{2d^2\lambda^2}{\pi\text{MFD}^2}. \tag{2}$$

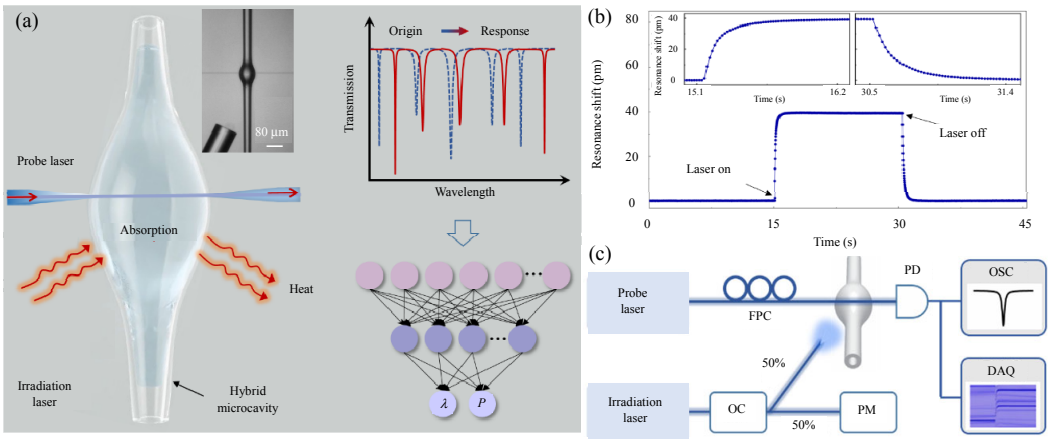

Fig. 1 Hybrid microcavity for multidimensional laser measurement: (a) schematic of the hybrid microcavity for multidimensional laser measurement, where the external irradiation laser irradiates the hybrid microcavity through a single mode fiber. The laser power and wavelength are decoupled via the machine learning method (inset: optical microscope images of the hybrid microcavity, coupling fiber, and irradiation fiber), (b) real-time response of the resonance shift under the irradiation of a 1 460 nm laser beam with the power of 1.5 mW [inset: zoom-in images of rising (left) and falling (right) processes in (b)], and (c) detailed experimental setup (FPC: fiber polarization controller; PD: photodetector; OSC: oscilloscope; DAQ: data acquisition card; OC: optical coupler; PM: power meter).

It can be observed from the equation that the spot area relies on the irradiation wavelength. Therefore, on the same experimental condition, even though the absorption of different wavelengths on both sides of the same absorption peak is identical, it will not induce the same effect due to the different irradiation laser spot areas. When the irradiation wavelength is 1 460 nm, the irradiation laser spot area of 890 μm^2 is calculated according to the theoretical equation, where the light absorption is highly localized, leading to rapid changes in temperature. As a result, the resonant mode experiences a sharp shift when the irradiation laser state changes, as shown in Fig. 1(b). The response time and recovery time are approximately 300 ms and 400 ms, respectively. This is a reversible process, and thus the hybrid microcavity also can be used for photosensitive switches. The detailed experimental setup is illustrated in Fig. 1(c). The probe laser at ~778 nm is efficiently coupled into the hybrid microcavity via a taper fiber. The taper fiber with transmittance over 90% is fabricated via "heating and pull" methods. There is no gap between the hybrid microcavity and taper fiber to ensure the stability of the measurement system. The irradiation laser at the near-infrared band irradiates the hybrid microcavity through a single-mode fiber. A fiber polarization controller is adopted to tune the polarization state to guarantee optimal coupling efficiency. The transmission light signal is received by a low-noise photodetector and monitored via an oscilloscope in the real time. A data acquisition card

is used for the real-time collection of transmission spectra. An optical coupler with a ratio of 50:50 is employed to divide the input laser, and thus the illuminated laser power can be in-lined monitored and calibrated through the reference optical path.

Figure 2(a) shows a representative transmission spectrum of a typical hybrid microcavity. It is obvious that the hybrid microcavity can maintain an ultrahigh Q-factor of ~4.5×10^7, even though the light absorption of infiltrated water can spoil the Q-factor. This is mainly due to the relatively major optical field confined in the silica wall, as shown in Fig. 2(b). Quantitatively, the electric field of the first-order radial mode is obtained by the finite-element-method simulation in COMSOL Multiphysics and about 99.94% of the light field is distributed inside the silica walls. Furthermore, the long-term stability of the hybrid microcavity is characterized, as displayed in Fig. 2(c). The standard deviation of the resonant wavelength shift over 10 min is approximately 0.04 pm, which is two orders of the magnitude smaller than the shift induced by the sensing signal. The whole experiment can be completed in 10 min, and thus the effects of environmental disturbance on experimental results can be ignored. In addition, the Allan variance is further calculated to reflect the intrinsic noise of the measurement system, as shown in the inset of Fig. 2(c). It is observed that the Allan variance first experiences a decline process, reaching a minimum at ~1 s, and subsequently starts to increase over time, which is mainly due to the thermal noise from the environment and probe laser. The laser frequency jitter can be compensated by monitoring the relative changes between different resonant modes of the transmission spectrum. Figure 2(d) compares the resonance shift of the hybrid and pure microcavities (i.e., the air-filled OMBR), both of which have resonant wavelengths close to 778 nm. The resonant mode of the hybrid microcavity exhibits the red-shift behavior with the irradiation laser power increasing. On the contrary, the pure microcavity remains almost unchanged, which is mainly due to the weak absorption of silica OMBR in near-infrared [41]. This phenomenon further demonstrates the feasibility of water-infiltrated hybrid microcavity in laser measurement.

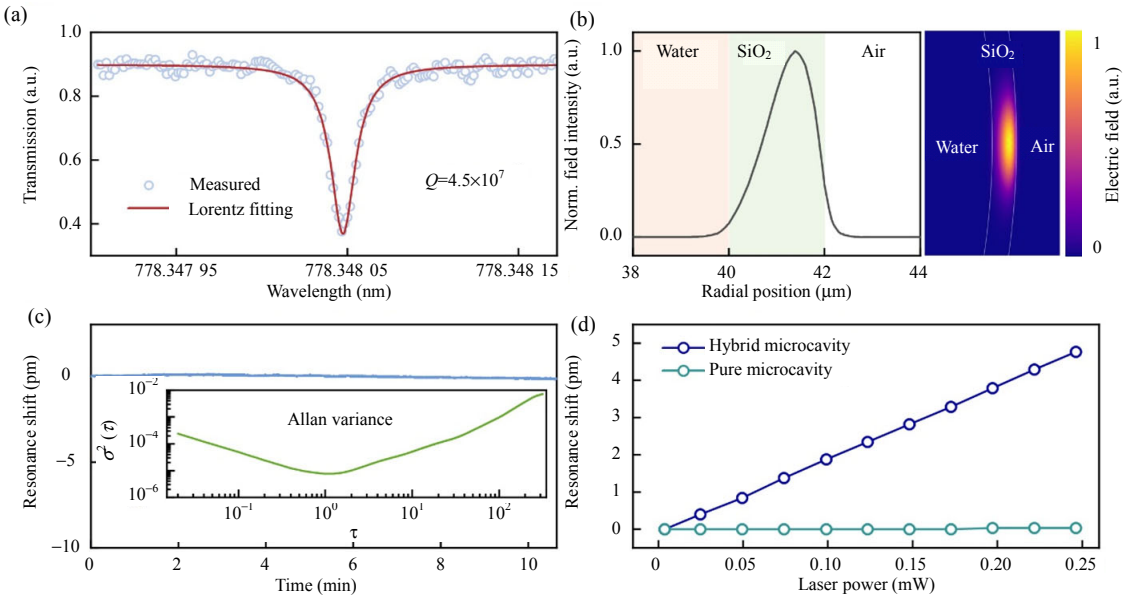

Fig. 2 Characterization of the hybrid microcavity: (a) transmission spectrum (hollow circle) of the hybrid microcavity [the typical Q-factor of 4.5×10^7 is obtained via Lorentz fitting (red line)], (b) electric field distribution of the first-order radial mode of the hybrid microcavity by the finite-element-method simulation, (c) long-term stability of the measurement system (inset: the Allan variance of the resonant wavelength), and (d) resonant wavelength shift of the hybrid (blue) and pure (green) microcavities as a function of irradiation light power at the irradiation wavelength of 1 490 nm.

3. Results and discussion

To evaluate the laser measurement performance of the hybrid microcavity, the evolved transmission spectra are monitored under 1 440 nm laser beam irradiation with different power, as displayed in Fig 3(a). Figure 3(b) shows the response of different resonant modes to laser power, and these modes exhibit various sensing characteristics due to the different light field distribution. The highest sensitivity of 59.95 pm/mW is obtained within the measurement range by linearly fitting the resonant wavelength changes [red region in Fig. 3(a)]. Figure 3(c) compares the dependence of the resonance shift on laser power with the irradiation wavelength ranging from 1 440 nm to 1 520 nm. The power sensitivities as a function of the irradiation laser wavelength are plotted in Fig. 3(d). It can be seen that the sensitivities exhibit nonlinear descending behavior with the increasing irradiation wavelength. This is mainly resulted from the decreased light absorption efficiency of water in the spectral bandwidth of 1 440 nm–1 520 nm [49]. To further investigate the wavelength dependence absorption of water, the response of the resonance shift on the irradiation laser wavelength is measured.

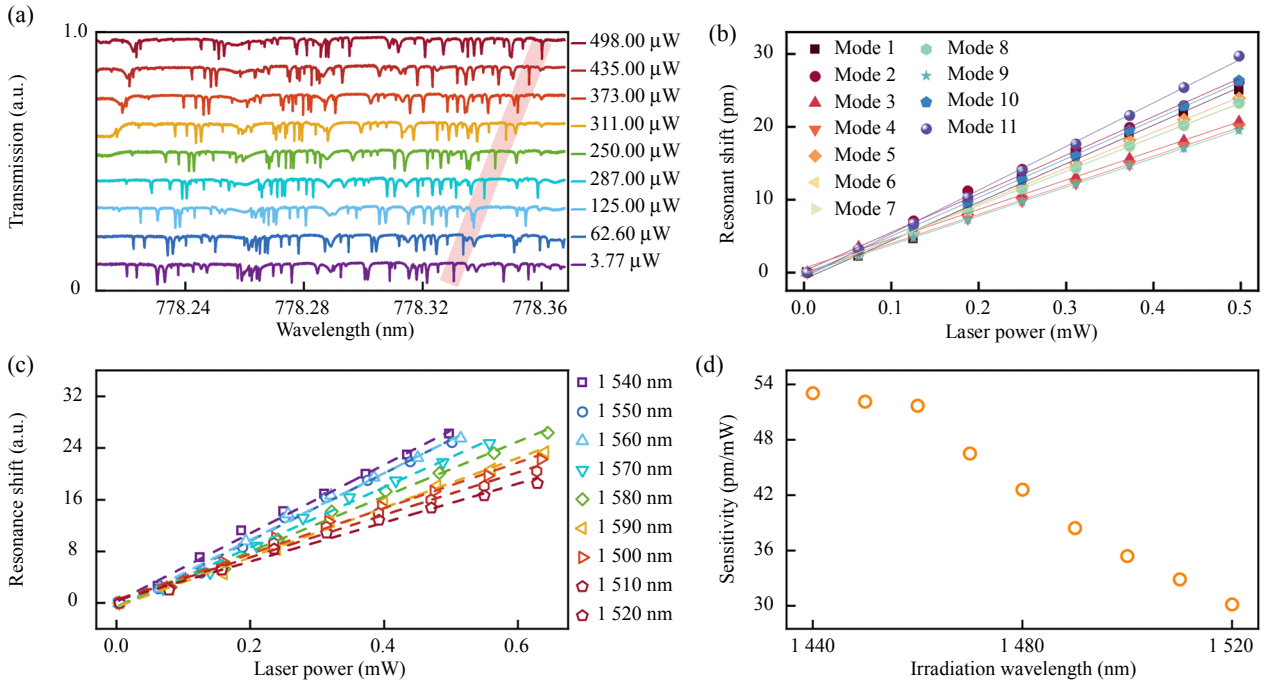

Fig. 3 Hybrid microcavity for laser power sensing: (a) transmission spectra evolution with irradiation laser power increasing when the irradiation wavelength is 1 440 nm, (b) sensing characteristics of different resonant modes in (a), and the highest sensitivity of 59.95 pm/mW is obtained by linearly fitting the resonant wavelength shift of the red region in (a), (c) dependence of the resonant wavelength shift on laser power for different irradiation wavelengths, and (d) laser power sensitivity versus the irradiation wavelength.

Figure 4(a) indicates the evolution of transmission spectra as the irradiation laser wavelength increases from 1 360 nm to 1 630 nm with an increment of 10 nm. The typical resonance shift (blue circle) as a function of the irradiation laser wavelength at the power of 0.5 mW is plotted in Fig. 4(b). It is observed that the resonance shift first suffers an increase process reaching a maximum of ~1 440 nm and then starts to decrease, matching well with the absorption spectrum of water [the red dashed line in Fig. 4(b)] [49]. The slight deviation may be due to the irradiation spot area variations at different irradiation wavelengths. It is noted that the absorption coefficient of water is two orders of magnitude higher in the longer wavelength band [inset of Fig. 4(b)] compared to the near-infrared, which suggests that the proposed hybrid-microcavity photosensor can be further

expanded to the mid-infrared, far infrared, and terahertz bands [50]. Furthermore, the real-time measurement capability of the hybrid microcavity is demonstrated. As expected, the resonance shift is observed when the irradiation light power and wavelength changes. Figure 4(c) shows the response of the hybrid microcavity under irradiation of the 1 550 nm laser beam with the power of 4.11 mW, 8.23 mW, 12.34 mW, and 16.57 mW. It is observed that the resonant wavelength can restore to the initial position when the power returns to the original value. In addition, the real-time response of the irradiation wavelength is plotted in Fig. 4(d). When the irradiation laser wavelength is scanned from 1 480 nm to 1 630 nm at a sweep rate of 4 nm/s, the resonance shift decreases and increases in the opposite process. Moreover, the corresponding resonance shifts almost equally in the rising and falling process, suggesting excellent reversibility.

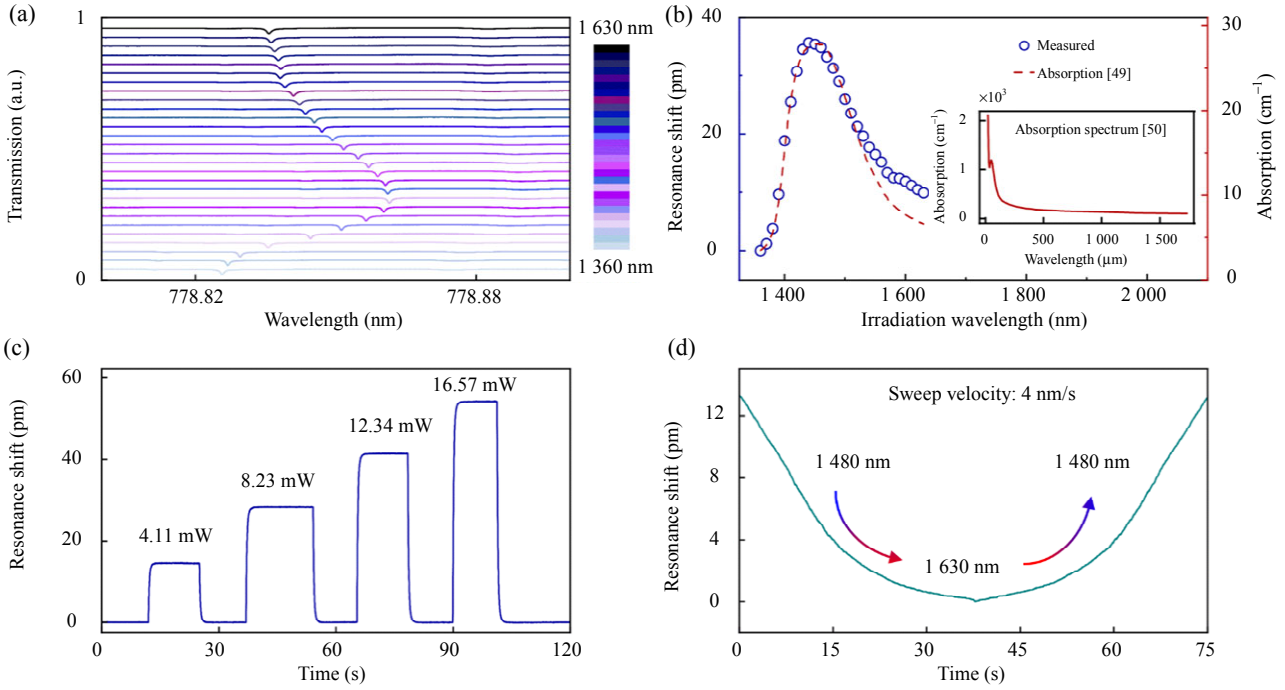

Fig. 4 Laser wavelength sensing performance and real-time response of the hybrid microcavity: (a) transmission spectra of the hybrid microcavity with the wavelength ranging from 1 360 nm to 1 630 nm in the step of 10 nm, (b) resonant wavelength shift as a function of the irradiation laser wavelength at the power of 0.5 mW (the red dashed line is the absorption spectrum of water). Inset: The absorption spectrum of water in the spectral bandwidth of 22.22 μm–1 733 μm, and the real-time response of the hybrid microcavity to the power (c) and wavelength (d) of irradiation.

From the above experimental results, it can be seen that the resonance shift shows significant power and wavelength dependence, and thus it is promising to realize the simultaneous measurement of the laser power and wavelength. The multi-parameter sensing matrix is a commonly used decoupling method, but this method strictly requires a linear relationship between the target parameters and sensing signal [51]. Moreover, this linear decoupling method is susceptive to the mode crosstalk, which significantly destroys the decoupling accuracy. Machine learning with powerful nonlinear modeling capabilities, enables a wide range of data-driven sensing applications, such as high-precision measurement and multicomponent analysis, offering a powerful tool to precisely decouple multiple parameters [52, 53]. Here, a three-layer perceptron neural network, including one input layer, one hidden layer, and one output layer, is adopted to decouple the power and wavelength, as

shown in Fig. 5(a). There are 100 nodes in the input layer, 50 nodes in the hidden layer, and 2 nodes in the output layer corresponding to the laser power and wavelength. The optimizer is set to the Adam optimizer with the learning rate of 0.000 1. The activated and loss functions are defined as the rectified linear units (ReLu) and mean square error (MSE), respectively. The dependence of the loss function on training iterations is plotted in Fig. 5(b). It is observed that with an increase in iterations, the loss significantly decreases and converges to around 3.6.

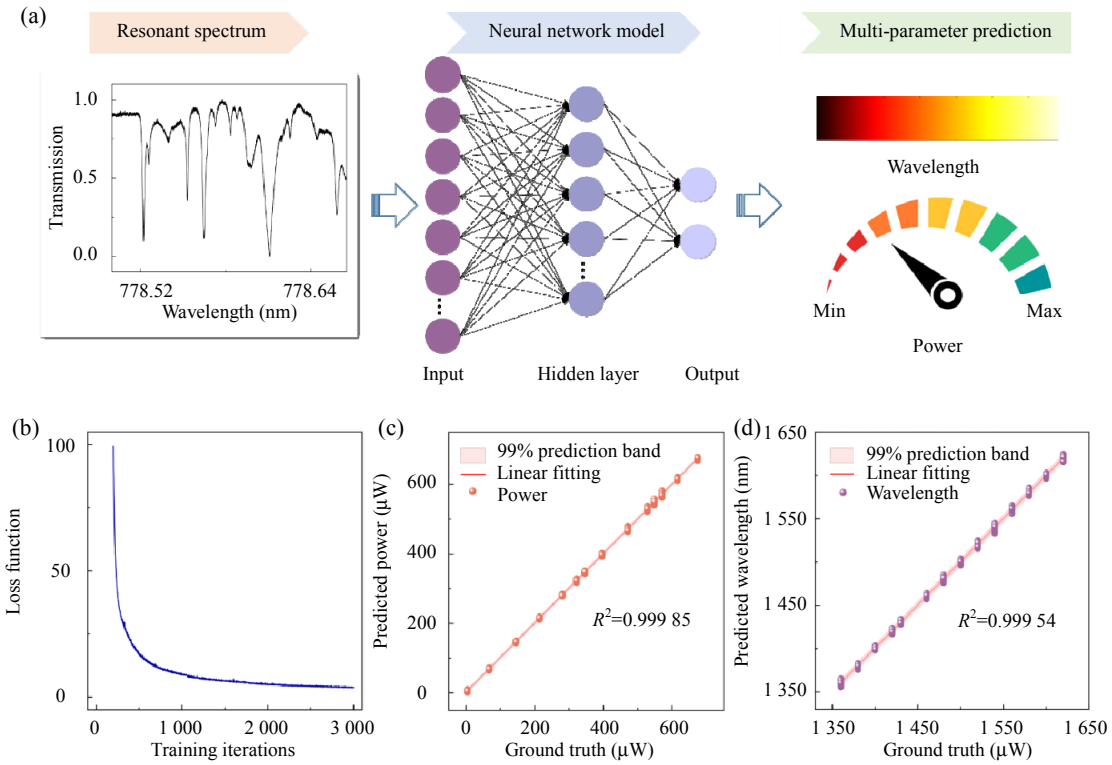

Fig. 5 Laser power and wavelength decoupling based on machine learning: (a) resonant spectrum with the unknown sample is fed into the neural network to predict the wavelength and power of the irradiation laser (the neurons of the input layer, hidden layer, and output layer are 100, 50, and 2, respectively), (b) the loss function (i.e., MSE) versus training iterations, and predictions versus the ground truth for the irradiation laser power (c) and wavelength (d).

Herein, the transmission spectra are collected for training and testing the neural network model. Experimentally, the transmission spectra are collected with the irradiation laser wavelength changing from 1 360 nm to 1 630 nm and power ranging from 4 μW to 674 μW. The typical measured time for the transmission spectrum is 20 ms, and the measurement system exhibits the good real-time capability. The wavelength range of the transmission spectra is about 0.17 nm, which is determined by the scanning range of the probe laser. The collected total dataset contains 6 264 samples, of which 4 698 samples are used to train the network model and 1 566 samples for blind testing. Each spectrum in the dataset is encoded with the laser power and wavelength. It is worth noting that the datasets with the high quality are collected due to the excellent stability of the experimental system, enabling satisfactory results with small datasets. The correlation coefficient R^2 is introduced to characterize prediction performance, which can be defined as [52]

$$R^2(y,\hat{y}) = 1 - \frac{\sum_{i=0}^{N-1}(\hat{y}_i - y_i)^2}{\sum_{i=0}^{N-1}(\bar{y}_i - y_i)^2} \tag{3}$$

where y_i and $\hat{y}_i$ are the ground truth and predictions, respectively, $\overline{y}_i$ is the average value of the ground truth, and N is the number of samples. The predicted irradiation laser power and wavelength for all testing samples against the measured values are plotted, as displayed in Figs. 5(c) and 5(d). The values of correlation coefficient R^2 of 0.999 85 and 0.999 54 are obtained for laser power and wavelength decoupling. The average prediction error for laser power is 2.16 μW with a standard deviation of 1.68 μW, and more than 84% of predictions have an error less than 4 μW. In the wavelength prediction, the average error of 1.43 nm with a standard deviation of 1.09 nm is achieved, with more than 85% of the predicted values having an error no greater than 2.5 nm. It can be observed that the relationship between the predictions (the laser power and wavelength) and ground truth (i.e., the expected values) exhibits the good linearity. Almost all the predictions fall in the 99% prediction band, indicating the ability of the neural network model for precise decoupling. The prediction accuracy can be further improved by selecting more photosensitive materials. Moreover, heterodyne interference can be used for noise cancellation to improve the prediction accuracy, which not only cancels the common mode noise, but also improves the spectral resolution by shifting the sensing signal from the optical band to the radio frequency band [54].

4. Conclusions

In summary, we demonstrate a novel multidimensional photosensor based on a water-infiltrated hybrid OMBR. We reveal that the laser power can be precisely measured by using photo-thermal conversion in a high-Q hybrid microcavity, and the intrinsic absorption spectrum of water allows for the wavelength-resolved measurement. With the assistance of machine learning, the laser power and wavelength are precisely decoupled with almost all predictions falling in the 99% prediction band, and the correlation coefficient R^2 greater than 0.999. It is worth mentioning that the proposed hybrid microcavity not only enables near-infrared laser measurement but also can be extended to mid-infrared and even terahertz bands due to the broad absorption spectrum of water. In addition, further research to optimize the algorithm is important for the generalization of machine learning to another hybrid OMBRs-based photosensor without a retraining process. This work lays the foundation for multidimensional laser measurement based on optical microcavities.

Acknowledgment

This work was supported by the National Key Research and Development Program, China (Grant No. SQ2023YFB2805600); Beijing Municipal Natural Science Foundation, China (Grant No. Z210004); National Natural Science Foundation of China (Grant Nos. 12474372 and 12474429); the Fundamental Research Funds for the Central Universities, China (Grant No. 2243300003); Beijing Nova Program from Beijing Municipal Science and Technology Commission, China (Grant No. 20230484433); State Key Laboratory of Information Photonics and Optical Communications, Beijing University of Posts and Telecommunications, China (Grant No. IPOC2021ZT01).

Declarations

Conflict of Interest The authors declare that they have no competing interests.

Permissions All the included figures, tables, or text passages that have already been published elsewhere have obtained the permission from the copyright owner(s) for both the print and online format.

indicate if changes were made.

References

[1] X. Y. Zhang, Q. T. Cao, Z. Wang, Y. X. Liu, C. W. Qiu, L. Yang, *et al*., "Symmetry-breaking-induced nonlinear optics at a microcavity surface," *Nature Photonics*, 2019, 13: 21–24.

[2] J. H. Chen, X. Q. Shen, S. J. Tang, Q. T. Cao, Q. H. Gong, and Y. F. Xiao, "Microcavity nonlinear optics with an organically functionalized surface," *Nature Photonics*, 2019, 123(17): 173902.

[3] Q. T. Cao, H. M. Wang, C. H. Dong, H. Jing, R. S. Liu, X. Chen, *et al*., "Experimental demonstration of spontaneous chirality in a nonlinear microresonator," *Physical Review Letters*, 2017, 118(3): 033901.

[4] S. Zhu, B. Xiao, B. Jiang, L. Shi, and X. Zhang, "Tunable Brillouin and Raman microlasers using hybrid microbottle resonators," *Nanophotonics*, 2019, 8(5): 931–940.

[5] M. Aspelmeyer, T. J. Kippenberg, and F. Marquardt, "Cavity optomechanics," *Reviews of Modern Physics*, 2014, 86(4): 1391–1452.

[6] J. Zhang, B. Peng, S. Kim, F. Monifi, X. F. Jiang, Y. H. Li, *et al*., "Optomechanical dissipative solitons," *Nature*, 2021, 600: 75–80.

[7] C. L. Zhu, Y. L. Liu, L. Yang, Y. X. Liu, and J. Zhang, "Synchronization in PT symmetric optomechanical resonators," *Photonics Research*, 2021, 9: 2152–2166.

[8] G. Anetsberger, R. Rivière, A. Schliesser, O. Arcizet, and T. J. Kippenberg, "Ultralow-dissipation optomechanical resonators on a chip," *Nature Photonics*, 2008, 2: 627–633.

[9] E. Verhagen, S. Deléglise, S. Weis, A. Schliesser, and T. J. Kippenberg, "Quantum coherent coupling of a mechanical oscillator to an optical cavity mode," *Nature*, 2012, 482: 63–67.

[10] J. C. Shi, Q. X. Ji, Q. T. Cao, Y. Yu, W. J. Liu, Q. H. Gong, *et al*., "Vibrational Kerr solitons in an optomechanical microresonator," *Physical Review Letters*, 2022, 128(7): 073901.

[11] Y. Zhang, Q. L. Wu, S. L. Su, Q. Lou, and C. X. Shan, *et al*., "Cavity quantum electrodynamics effects with nitrogen vacancy center spins coupled to room temperature microwave resonators," *Physical Review Letters*, 2022, 128(25): 253601.

[12] L. Yao, P. Liu, H. J. Chen, Q. H. Gong, Q. F. Yang, and Y. F. Xiao, *et al*., "Soliton microwave oscillators using oversized billion *Q* optical microresonators," *Optica*, 2022, 9: 561–564.

[13] H. Zhang, T. Tan, H. J. Chen, Y. Yu, W. T. Wang, B. Chang, *et al*., "Soliton microcombs multiplexing using intracavitystimulated Brillouin lasers," *Physical Review Letters*, 2023, 130(15): 153802.

[14] Ó. B. Helgason, M. Girardi, Z. C. Ye, F. C. Lei, J. Schröder, and V. Torres-Company, "Surpassing the nonlinear conversion efficiency of soliton microcombs," *Nature Photonics*, 2023, 17: 992–999.

[15] X. Yang, S. J. Tang, J. W. Meng, P. J. Zhang, Y. L. Chen, Y. F. Xiao, "Phase-transition microcavity laser," *Nano Letters*, 2023, 23(7): 3048–3053.

[16] L. He, Ş. K. Özdemir, and L. Yang, "Whispering gallery microcavity lasers," *Laser & Photonics Reviews*, 2013, 7(1): 60–82.

[17] W. J. Wang, C. H. Zhou, T. T. Zhang, J. D. Chen, S. D. Liu, and X. D. Fan, "Optofluidic laser array based on stable high-*Q* Fabry-Pérot microcavities," *Lab on a Chip*, 2015, 15(19): 3862–3869.

[18] Y. Zhi, X. C. Yu, Q. Gong, L. Yang, and Y. F. Xiao, "Single nanoparticle detection using optical microcavities," *Advanced Materials*, 2017, 29(12): 1604920.

[19] T. Tan, Z. Y. Yuan, H. Zhang, G. F. Yan, S. Y. Zhou, N. An, *et al*., "Multispecies and individual gas molecule detection using stokes solitons in a graphene over-modal microresonator," *Nature Communications*, 2021, 12: 6716.

[20] S. Wan, R. Niu, H. L. Ren, C. L. Zou, G. C. Guo, and C. H. Dong, "Experimental demonstration of dissipative sensing in a self-interference microring resonator," *Photonics Research*, 2018, 6: 681–685.

[21] J. Su, A. F. Goldberg, and B. M. Stoltz, "Label-free detection of single nanoparticles and biological molecules using microtoroid optical resonators," *Light: Science & Applications*, 2016, 5: e16001.

[22] B. Yao, S. W. Huang, Y. Liu, A. K. Vinod, C. Choi, M. Hoff, *et al*., "Gate-tunable frequency combs in graphene-nitride microresonators," *Nature*, 2018, 558: 410–414.

[23] H. Zhang, L. Zhou, J. Xu, L. Lu, J. Chen, and B. M. A. Rahman, "All-optical non-volatile tuning of an AMZI-coupled ring resonator with GST phase-change material," *Optics Letters*, 2018, 43(22): 5539–5542.

[24] M. Rudé, J. Pello, R. E. Simpson, J. Osmond, G. Roelkens, J. J. van der Tol, *et al.*, "Optical switching at 1.55 μm in silicon racetrack resonators using phase change materials," *Applied Physics Lette*rs, 2013, 103(14): 141119.

[25] B. Yao, C. Yu, Y. Wu, S. W. Huang, H. Wu, Y. Gong, *et al.*, "Graphene-enhanced Brillouin optomechanical microresonator for ultrasensitive gas detection," *Nano Letters*, 2017, 17(8): 4996–5002.

[26] X. Jiang, A. J. Qavi, S. H. Huang, and L. Yang, "Whispering-gallery sensors," *Matter*, 2020, 3(2): 371–392.

[27] J. Liu, F. Bo, L. Chang, C. H. Dong, X. Ou, B. Regan, *et al*., "Emerging material platforms for integrated microcavity photonics," *Science China Physics*, 2022, 65(10): 104201.

[28] S. J. Tang, Z. Liu, Y. J. Qian, K. Shi, Y. Sun, C. Wu, *et al*., "A tunable optofluidic microlaser in a

photostable conjugated polymer," *Advanced Materials*, 2018, 30(50): 1804556.
[29] Y. Yang, F. Lei, S. Kasumie, L. Xu, J. M. Ward, L. Yang, *et al*., "Tunable erbium-doped microbubble laser fabricated by sol-gel coating," *Optics Express*, 2017, 25(2): 1308–1313.
[30] Z. Feng and L. Bai, "Advances of optofluidic microcavities for microlasers and biosensors," *Micromachines*, 2018, 9(3): 122.
[31] X. C. Yu, S. J. Tang, W. Liu, Y. Xu, Q. Gong, Y. L. Chen, *et al*., "Single-molecule optofluidic microsensor with interface whispering gallery modes," *Proceedings of the National Academy of Sciences*, 2022, 119(6): e2108678119.
[32] Z. Cao, B. Yao, C. Qin, R. Yang, Y. Guo, Y. Zhang, *et al*., "Biochemical sensing in graphene-enhanced microfiber resonators with individual molecule sensitivity and selectivity," *Light: Science & Applications*, 2019, 8: 107.
[33] D. Q. Yang, J. H. Chen, Q. T. Cao, B. Duan, H. J. Chen, X. C. Yu, *et al*., "Operando monitoring transition dynamics of responsive polymer using optofluidic microcavities," *Light: Science & Applications*, 2021, 10: 128.
[34] X. Zhao, Z. Guo, Y. Zhou, J. Guo, Z. Liu, Y. Li, *et al*., "Optical whispering-gallery-mode microbubble sensors," *Micromachines*, 2022, 13(4): 592.
[35] D. Yu, M. Humar, K. Meserve, R. C. Bailey, S. N. Chormaic, and F. Vollmer, "Whispering-gallery-mode sensors for biological and physical sensing," *Nature Reviews Methods Primers*, 2021, 1(1): 83.
[36] N. Toropov, G. Cabello, M. P. Serrano, R. R. Gutha, M. Rafti, and F. Vollmer, "Review of biosensing with whispering-gallery mode lasers," *Light: Science & Applications*, 2021, 10: 42.
[37] D. Yang, A. Wang, J. H. Chen, X. C. Yu, C. Lan, Y. Ji, *et al*., "Real-time monitoring of hydrogel phase transition in an ultrahigh *Q* microbubble resonator," *Photonics Research*, 2020, 8(4): 497–502.
[38] J. Liao and L. Yang, "Optical whispering-gallery mode barcodes for high-precision and wide-range temperature measurements," *Light: Science & Applications*, 2021, 10(1): 32.
[39] W. Liu, W. Li, R. Wang, E. B. Xing, N. Jing, Y. R. Zhou, *et al.*, "Magnetic sensor based on WGM hollow microbubble resonator filled with magnetic fluid," *Optics Communications*, 2021, 497: 127148.
[40] L. Fu, Q. Lu, X. Liu, X. Chen, X. Wu, and S. S. Xie, "Combining whispering gallery mode optofluidic microbubble resonator sensor with GR-5 DNAzyme for ultra-sensitive lead ion detection," *Talanta*, 2020, 213: 120815.
[41] S. K. Zhu, Z. H. Zheng, W. Meng, S. S. Chang, Y. Tan, L. J. Chen, *et al*., "Harnessing disordered photonics via multi-task learning towards intelligent four-dimensional light field sensors," *PhotoniX*, 2023, 4(1): 26.
[42] S. Yuan, C. Ma, E. Fetaya, T. Mueller, D. Naveh, F. Zhang, *et al*., "Geometric deep optical sensing," *Science*, 2023, 379(6637): eade1220.
[43] C. Ma, S. Yuan, P. Cheung, K. Watanabe, T. Taniguchi, F. Zhang, *et al*., "Intelligent infrared sensing enabled by tunable moiré quantum geometry," *Nature*, 2022, 604(7905): 266–272.
[44] J. Wei, C. Xu, B. Dong, C. W. Qiu, and C. Lee, "Mid-infrared semimetal polarization detectors with configurable polarity transition," *Nature Photonics*, 2021, 15(8): 614–621.
[45] B. Wozniak and J. Dera, "*Light Absorption by Suspended Particulate Matter (SPM) in Sea Water,*" New York: Springer, 2007, pp:167–294.
[46] D. Yang, B. Duan, A. Wang, Y. Pan, C. Wang, Y. Ji, *et al*., "Packaged microbubble resonator for versatile optical sensing," *Journal of Lightwave Technology*, 2020, 38(16): 4555–4559.
[47] J. Yang, Y. Zhuang, W. Shen, and Z. Lin, "Precise measurement of the effective area of laser spot," *Collection of Theses on High Power Laser and Plasma Physics*, 2004, 2(1): 83–86.
[48] J. D. Musgraves, J. Hu, and L. Calvez, "*Springer Handbook of Glass*," Cham: Springer Nature, 2019.
[49] S. Kedenburg, M. Vieweg, T. Gissibl, and H. Giessen, "Linear refractive index and absorption measurements of nonlinear optical liquids in the visible and nearinfrared spectral region," *Optical Materials Express*, 2012, 2(11): 1588–1611.
[50] M. N. Afsar and J. B. Hasted, "Measurements of the optical constants of liquid H_2O and D_2O between 6 and 450 cm^{-1}," *Journal of the Optical Society of America*, 1977, 67(7): 902–904.
[51] Y. Wu, B. Duan, J. Song, H. Tian, J. H. Chen, D. Yang, *et al*., "Simultaneous temperature and pressure sensing based on a single optical resonator," *Optics Express*, 2023, 31(12): 18851–18861.
[52] B. Duan, H. Zou, J. H. Chen, C. H. Ma, X. Zhao, X. Zheng, *et al*., "High-precision whispering gallery microsensors with ergodic spectra empowered by machine learning," *Photonics Research*, 2022, 10(10): 2343–2348.
[53] Z. Li, H. Zhang, B. T. T. Nguyen, S. Luo, P. Y. Liu, J. Zou, *et al*., "Smart ring resonator-based sensor for multicomponent chemical analysis via machine learning," *Photonics Research*, 2021, 9(2): B38–B44.
[54] Y. Wang, Y. Li, Y. Li, H. Zhang, Z. Liu, Y. Guo, *et al.,* "Noise canceled graphene- microcavity fiber laser sensor for ultrasensitive gas detection," *Photonics Research*, 2023, 11(8): A1–A9.